


Article

Evaluation of Effectiveness of CO₂ Sequestration Using Portland Cement in Geological Reservoir Based on Unified Pipe-network Method

Xiao Yan ^{1,2}, Zizheng Sun ^{3,*}, Shucaï Li ³, Weimin Yang ³ and Yiming Zhang ^{4,*} 

¹ State Key Laboratory for Geo-mechanics and Deep Underground Engineering, China University of Mining and Technology, 1 Daxue Road, Xuzhou 221116, China; Xiao.Yan@ruhr-uni-bochum.de

² Institute for Structural Mechanics, Ruhr University Bochum, Universitätsstraße 150, 44801 Bochum, Germany

³ Geotechnical & Structural Engineering Research Center, Shandong University, Jinan 250061, China; lishucaï@sdu.edu.cn (S.L.); weimin.yang@sdu.edu.cn (W.Y.)

⁴ School of Civil and Transportation Engineering, Hebei University of Technology, 5340 Xiping Road, Beichen District, Tianjin 300401, China

* Correspondence: zizheng.sun@sdu.edu.cn (Z.S.); yiming.zhang@hebut.edu.cn (Y.Z.)

Received: 29 October 2019; Accepted: 17 December 2019; Published: 13 January 2020



Abstract: In this paper, we first recapitulate some basic notions of the CO₂ sequestration and numerical model. Next, a mixed model is employed into the CO₂ sequestration framework, for simulating CO₂ geological sequestration processes. The last part of the paper makes extensions to evaluation of the effectiveness of CO₂ sequestration with respect to atmospheric pressure, formation temperature, the initial reactant concentration, fracture aperture, and fracture dip. The results show that reactive Portland cement has a great impact on the effectiveness of CO₂ sequestration, while the proposed mixed model is robust in simulation.

Keywords: CO₂ sequestration; multi-field analysis; unified pipe-network method; reactive portland cement

1. Introduction

Anthropogenic emissions of carbon dioxide (CO₂) lead to global warming, and many other serious problems, i.e., extreme weather and disease, wreak havoc. Considering both the cost and efficiency of the storage methods, CO₂ geological sequestration is regarded as a effective way to reduce the release of CO₂ to the atmosphere. However, specific conditions are required to construct the reservoir of CO₂, one of which is an impermeable seal overlying the reservoir. Hence, some measures should be implemented due to the the existence of discrete fracture networks. As one of the most effective methods, using CO₂-reactive or CO₂-consuming solution to form precipitation clogging the voids of the formation to reduce the porosity and hydraulic conductivity of the rock and minimize CO₂ emission have been developed [1–5]. Thus, it's very important to evaluate the effectiveness of CO₂ sequestration using portland cement in geological reservoir.

Portland cement will react with CO₂ when water is present and form carbonation [6]. Carbonation is associated with the changes in the flow and transport properties and will cause to a loss of hydraulic and diffusion properties [6–11]. The change of porosity in porous medium are typically caused by the mineral alteration processes. During chemical or physical process, clogging of porous media due to mineral precipitation can lead to a reduction of the effective porosity and hydraulic conductivity. In addition, different reaction rates will cause local concentration gradients

and different transport path in connected pores, which are strongly dependent upon pore-scale heterogeneity [12,13]. Researchers have experimentally investigated the effect of microstructure changes on permeability and porosity due to dissolution or precipitation at the pore scale [14–16]. These studies found that the reaction rates are strongly related with the pore-scale conditions [17–19]; moreover, the spatial distribution of total reaction rates in the pore space is non-uniform [20–24]. Nonetheless, while the experimental results propose some reasonable connection between porosity and permeability, they are not transferable on the long term since the experiments can only be lasted for several months, furthermore, reactive transport codes for predicting the evolution process are not experimentally accessible in space and time [25–28].

For simulating the geochemical processes in long-term period of CO₂ sequestration, numerical methods [29–31], including finite difference method (FDM) [32,33], finite element method (FEM) [34–37], finite volume method (FVM) [38], smoothed particle hydrodynamics (SPH), lattice Boltzmann methods (LBM), have been proposed to solving the energy, momentum and concentration conservation equations [39]. With these methods, many studies are carried out, for insurance, Luo [40] et al. and Tartakovsky [24] et al. simulate the reactive transport and precipitation process in porous media and analyzed the effective reaction coefficients and mass transfer coefficients [17,41,42]. Parmigiani et al. [43] used LBM to simulate the multiphase reactive transport and reaction process in the random pore media and studied the spatial distribution of each phase. However, it is arduous for computer programming that requires a considerable use of parallel computing approaches and it is difficult to add the constant-pressure boundary conditions.

Most numerical models assume that CO₂ is evenly released into the aquifer, and neglect the influence of fractures on CO₂ sequestration. However, the permeability of fractures are much larger than the rock matrix, which should be treated as channels in fractured porous media for fluid flow and reactive transport [44,45]. The fractures are significant in prediction of CO₂ leakage evolution and distribution. Research has been presented on the simulation of fractured model, i.e., Bigi et al. [46] build a fractured model to study the CO₂ emission through fracture networks by establishing the Analogue Models. Lee [47] investigated CO₂ injection process in fractured formation. Pan et al. [48] analyzed the initial 2D caprock failure induced by geologic carbon sequestration. They all emphasize the importance of fractures on the CO₂ leakage. The discrete models are regarded as an effective tool to understand the release of CO₂. However, most of the models were generally simulated within 2D domains due to the computational complexity and demand. Although 2D models are useful to analyze the CO₂ sequestration in fractured rock, they are not able to fully represent a geological formation with all its complexities, so they cannot accurately capture the CO₂ release and distribution.

The present study aims to simulate the CO₂ sequestration in the 3D domain considering the existence of fracture networks in the caprock. This process couples the process of fluid flow, reactive solute transport and chemical reaction. The unified pipe-network method (UPM) [49–52] is employed for its simpleness in the simulation of mass/energy-transport in 3D fractured rock matrix. The fluid pressure, reactive solute concentration and chemical reaction rate are assigned to each node. With this methodology, the Darcy scale model and the pore-scale model can be solved together. The UPM solves the coupled transport equations one after another and transfers the field states among different physical/chemical fields back and forth, avoiding strong coupled description of the multi-fields such as [53–57]. Moreover, the simulations of crack initiation and propagation are not considered, avoiding complex models presented in such as [58–66]. The UPM transforms 3D complicated fractures and porous medium into 1D artificial connected pipes in domain space and it uses the equivalent pipe networks to simulate the mass/energy transport processes within a 3D fractured porous medium. The properties of pipes are obtained according to the geometrical, hydraulic and transport properties of the corresponding fractures and rock matrices. Thus, the 3D fractures with arbitrary geometric parameters can be established and embedded into the rock matrix.

Some basic assumptions of this model need to be firstly clarified as: (1) CO₂ sequestration can be regarded as a single phase flow process, as the gas phase is assumed to be immobile and is considered

as a fixed species neglecting the two-phase flow effects [67]; (2) the gaseous carbon dioxide CO₂ is converted into reactive liquid CO₂ and then analyze the transport of the dissolved CO₂ and the precipitation process of minerals without considering the CO₂ dissolution; (3) the distribution of pore in the porous medium is regarded to be uniform.

In this paper, we will first review some basic concepts in CO₂ sequestration and grouting seepage prevention, and in mixed modeling. Next, we will employ the mixed model to simulate the CO₂ sequestration in the 3D domain considering the existence of fracture networks, where we investigate a number of factors that can critically affect the performance of mixed model in CO₂ sequestration. A contribution on how to apply mixed model to sequestering CO₂ follows in Section 4. Variation of CO₂ concentration, Si concentration, and porosity are considered. Conclusions drawn from this simulation are presented in Section 5.

2. Methodology

2.1. Description of the Reactive Transport Code

In this paper, we consider a simplified chemical model to analyze the process of reactant transport in porous medium, while the chemical model can be described with two aqueous chemical species and one solid phase as:



where *aq* stands for aqueous species, and *s* refers to solid phase. Equation (1) is a precipitation reaction in which the aqueous *A*_(aq) reacts with aqueous *B*_(aq), generating the precipitate *C*_(s).

The incompressible saturated fluid flow in porous media and fractures can be described by a mass balance equation:

$$\frac{\partial}{\partial t}(\phi^\tau \rho) + \nabla \cdot (\rho \frac{1}{\mu} K^\tau \cdot \nabla P) = \rho q, \quad (2)$$

where τ is a term to express the matrix and fracture, respectively ($\tau = m$ represents matrix and $\tau = f$ represents fracture); ϕ is the porosity; K is the intrinsic permeability tensor (m²); ρ is the fluid density (kg m⁻³); μ is the fluid viscosity (Pa·s); P is the fluid pressure (Pa); and q is the source term. Assuming that the fracture is smooth and parallel and the fluid flow obeys the cubic law, the intrinsic permeability for fracture can be estimated as $k^f = a^2/12$, where a is the fracture aperture (m) [68].

The governing equation of transport of aqueous chemical species in rock matrix and fracture are established based the advection-diffusion equation [4]:

$$\frac{\partial}{\partial t}(\phi^\tau C) + \vec{u} \cdot \nabla C = \nabla \cdot (\phi^\tau D^\tau \cdot \nabla C) + r, \quad (3)$$

where C is the concentration of the solute (mol m⁻³); \vec{u} is the reactant solution velocity vector (m s⁻¹); D^τ is the molecular diffusion–dispersion coefficient of the chemical reactor (m² s⁻¹); r is the total reaction rate (mol m⁻³ s⁻¹); $r < 0$ represents the dissolution; and $r > 0$ represents the precipitation.

The precipitation growth in this model is described by surface reaction. The reaction of *A*_(aq) and *B*_(aq) on the surface of precipitation node causes the consumption of chemical reactant species in the pore and the growth of mineral product. The reaction kinetics at fluid-solid interface is expressed as [69]:

$$D_{A_{(aq)}} \frac{\partial C_{A_{(aq)}}}{\partial n} = \begin{cases} 0 & \text{if } C_{A_{(aq)}} C_{B_{(aq)}} < K_c \\ -k_r(1 - K_{eq} C_{A_{(aq)}} C_{B_{(aq)}}) & \text{if } C_{A_{(aq)}} C_{B_{(aq)}} \geq K_c \end{cases}, \quad (4)$$

$$D_{B_{(aq)}} \frac{\partial C_{B_{(aq)}}}{\partial n} = \begin{cases} 0 & \text{if } C_{A_{(aq)}} C_{B_{(aq)}} < K_c \\ -k_r(1 - K_{eq} C_{A_{(aq)}} C_{B_{(aq)}}) & \text{if } C_{A_{(aq)}} C_{B_{(aq)}} \geq K_c \end{cases}, \quad (5)$$

where k_r is the reaction rate constant ($\text{mol m}^{-2} \text{s}^{-1}$); K_{eq} is the equilibrium constant for reaction ($\text{m}^6 \text{mol}^{-2}$); and K_c is a threshold for denoting the mineral growth barrier on the surface of $C_{(s)}$ ($\text{mol}^2 \text{m}^{-6}$). The total reaction rate can be expressed as:

$$r = -Ak_r(1 - K_{eq}C_{A(aq)}C_{B(aq)}), \quad (6)$$

where A is the specific reactive surface area ($\text{m}^2 \text{m}^{-3} \text{rock}$).

The reaction rate constant k_r in Equations (4) and (5) is influenced by temperature, and the value at random temperature $T(K)$ can be calculated via the Arrhenius equation as [70,71]:

$$k_r = k_{25} \exp\left[-\frac{E_a}{R}\left(\frac{1}{T} - \frac{1}{298.15}\right)\right], \quad (7)$$

where k_{25} is the rate constant at 25 °C ($\text{mol m}^{-2} \text{s}^{-1}$); E_a is the activation energy (J mol^{-1}); and R is the gas constant ($\text{J mol}^{-1} \text{K}^{-1}$).

Precipitation of minerals leads to a increase of solid phase. The volume fraction of minerals β is updated by [41,72]:

$$\frac{\partial \beta}{\partial t} = -V_m Ak_r(1 - K_{eq}C_{A(aq)}C_{B(aq)}), \quad (8)$$

where V_m is the molar volume ($\text{m}^3 \text{mol}^{-1}$).

The change of volume fraction of solid phase due to precipitation directly causes the variation of porosity of rock matrix as [73]:

$$\phi^m = \phi_0^m - \sum_{i=1}^{N_m} \beta_i, \quad (9)$$

where ϕ_0^m is the initial matrix porosity and N_m represents the total mineral product.

Change of intrinsic permeability [74] and specific surface area [75] for the rock matrix is related to the porosity and can be estimated as:

$$\frac{K^m}{K_0^m} = \left(\frac{\phi^m - \phi_c^m}{\phi_0^m - \phi_c^m}\right)^n, \quad (10)$$

$$\frac{A}{A_0} = \left(\frac{1 - \phi^m}{1 - \phi_0^m}\right)^{\frac{2}{3}}, \quad (11)$$

where K_0^m is the initial intrinsic porosity tensor for matrix; A_0 is the initial specific surface area; ϕ_c^m is a “critical” porosity in which the matrix permeability approaches to zero; and n is a power law exponent.

2.2. UPM Model for Solute Transport

The Unified Pipe-Network Method based on the Control Volume Finite Element (CVFE) is proposed by Ren [49,50,76,77]; for a detailed description of this model, see [78,79]. In the UPM frame, the above mentioned two governing equations for both rock matrix and fractures are discretized as:

$$\frac{\partial(\phi_i^\tau V_i^\tau \rho)}{\partial t} + \rho \sum_{j=1}^{n_i} K_{ij}^\tau (P_i - P_j) = \rho Q_{s_i}, \quad (12)$$

$$\frac{\partial(\phi_i^\tau V_i^\tau C_i)}{\partial t} + \sum_{j=1}^{n_i} D_{ij}^\tau (C_i - C_j) + \sum_{j=1}^{n_i} Q_{ij} \left(\frac{C_i + C_j}{2}\right) + k_r A V_i^\tau (1 - K_{eq} C_{A(aq)} C_{B(aq)}) = 0, \quad (13)$$

where P_i and P_j are the pressures at node i and j ; and C_i and C_j are the concentrations for nodes i and j , respectively; ϕ_i^m is the porosity of node i ; V_i is the control volume of node i ; the subscript n_i is the total number of connected pipes; K_{ij}^m is the equivalent conductance coefficient of pipe ij ; and Q_{s_i} is the source term of node i . Q_{ij} is the flow rate of pipe ij .

The equivalent conductance coefficient of matrix pipe and fracture pipe ij can be expressed, respectively, as (the detailed derivation of these coefficient can be found in Appendices A and B):

$$K_{ij}^m = \frac{A_{oc1fc2} K_i^m}{l_{ij} \mu}, \quad (14)$$

$$K_{ij}^f = \frac{A_{of} K_i^f}{l_{ij} \mu} = \frac{l_{of} a^3}{l_{ij} \mu}, \quad (15)$$

where A_{oc1fc2} is the area of the face $oc1fc2$; A_{of} is the area of the face of ; and l_{ij} is the length of pipe ij . Similarly, the effective diffusion coefficient can be calculated as:

$$D_{ij}^m = \frac{\phi_i^m A_{oc1fc2} D_i^m}{l_{ij}}, \quad (16)$$

$$D_{ij}^f = \frac{\phi_i^f A_{of} D_i^f}{l_{ij}} = \frac{\phi_i^f l_{of} D_i^f a}{l_{ij}}. \quad (17)$$

2.3. Calculation of Chemical Reaction

In the current chemical precipitation process, the total reaction rate r is controlled by the concentration of both $A_{(aq)}$ and $B_{(aq)}$, which are two unknowns at the governing equation. In order to simplify the algorithm, a semi-explicit solution is used in this method to solve the total reaction rate. For the irreversible reaction $A_{(aq)} + B_{(aq)} \rightarrow C_{(s)}$, the reaction rate r can also be defined as proposed by Poskożim [80]:

$$r = \frac{dC_c}{dt} = -\frac{dC_A}{dt} = -\frac{dC_B}{dt}. \quad (18)$$

The average reaction rate is calculated as:

$$r \cdot \Delta t = \left(\frac{r(t) + r(t + \Delta t)}{2} \right) \cdot \Delta t, \quad (19)$$

where Δt is the time step (s). It is assumed that the average reaction rate can be regarded as the reaction rate at the next time step when the time step is little enough. Combined with Equations (18) and (19), the reaction rate at the next time step is expressed:

$$r(t + \Delta t) = -Ak_r(1 - K_{eq}C_{A_{aq}}(t + \Delta t)C_{B_{aq}}(t + \Delta t)) = -Ak_r(1 - K_{eq}(C_{A_{aq}}(t) - r)(C_{B_{aq}}(t) - r)). \quad (20)$$

Based on the Newton–Raphson method, the accurate total reaction rate r can be obtained.

3. Validation

In this section, we first present the validation for the UPM-based chemical reaction module in porous medium. The simulation results of the homogeneous chemical reaction $D_{(aq)} + M_{(aq)} \rightarrow P_{(aq)}$ are contrasted with analytical solutions of reaction in a free fluid. Moreover, additional models in the above UPM-based mix model (fluid flow problem and hydraulic-transport coupling problem) have been validated in [78,79]. Due to the quasi-implicit method used in our model, a convergence test is conducted to consider the influence of time step on the final results. The effects of operational factors (atmospheric pressure and reactive temperature), materials factors (reactant concentration), and geometry factors (fracture aperture and fracture dip) are discussed in a sensitivity analysis, thereby analyzing the influence of precipitation on the whole reaction.

3.1. Homogeneous Reaction in Porous Media

For the homogeneous reaction $D_{(aq)} + M_{(aq)} \rightarrow P_{(aq)}$, the total reaction rate can be written as [72]:

$$r = \kappa C_D C_M, \quad (21)$$

where κ is the homogeneous reaction rate constant ($\text{m}^3 \text{mol}^{-1} \text{s}^{-1}$). The analytical solutions for the concentration of species D and M in a batch system given by [81] are:

$$C_D = \frac{\Delta C_{DM} \cdot \frac{C_{D0}}{C_{M0}} \cdot e^{\kappa t \Delta C_{DM}}}{\left[\frac{C_{D0}}{C_{M0}} \cdot e^{\kappa t \Delta C_{DM}} - 1 \right]}, \quad (22)$$

$$C_E = \frac{\Delta C_{DM}}{\left[\frac{C_{D0}}{C_{M0}} \cdot e^{\kappa t \Delta C_{DM}} - 1 \right]}, \quad (23)$$

where C_{D0} and C_{M0} represents the initial concentration of reactant D and M , respectively; ΔC_{DM} is a constant and defined as $\Delta C_{DM} = C_{D0} - C_{M0}$.

In this comparison model, C_{D0} is $3.65 \times 10^{-12} \text{ mol/m}^3$, and C_{M0} is $1.78 \times 10^{-12} \text{ mol/m}^3$. Two dimensionless parameters (the dimensionless time $t_D = \kappa t \Delta C_{DM}$ and the dimensionless concentration $C_D = \frac{C}{C_{D0} + C_{M0}}$) are defined. Figure 1 compares the variations in concentrations of reactant and product obtained by analytical results and simulation results. It shows that the aforementioned method has a high degree of accuracy in predicting the change in concentration.

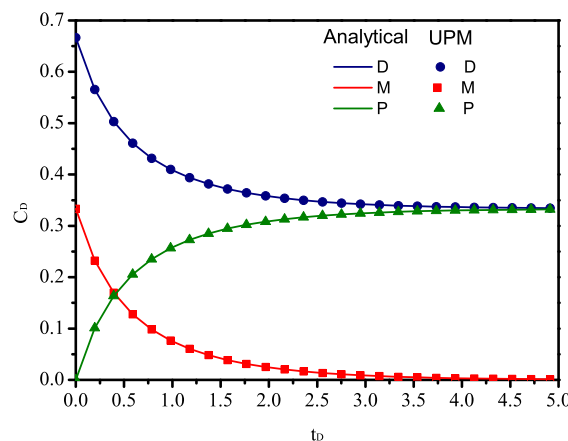


Figure 1. The variations of dimensionless concentration C_D of reactant and product with dimensionless time t_D .

3.2. Precipitation Reaction in Fractured Porous Media

The existence of a high permeable fracture embedded into the caprock may lead to the significantly leakage of CO_2 . The injection of appropriate reactive grout into the aquifer overlying the caprock filling with the pores around the fracture is regarded as an effective method to remedy the CO_2 leakage, as shown in Figure 2. In order to simulate this process, a 3 m thick caprock, with a single fracture throughout it, in a cube with dimensions of $(10 \text{ m} \times 10 \text{ m} \times 10 \text{ m})$ is modeled, as shown in Figure 3. Initially, the pores above the caprock are full of the reactive grout in advance of the occurrence of CO_2 leakage. The concentration of reactive chemical species Si in the solution is 2720 mol/m^3 [73]. The whole domain is set with a constant temperature (25°C). The atmospheric pressure on the top boundary is 10 bar. CO_2 leakage at a constant flow velocity ($1.25 \times 10^{-5} \text{ m/s}$) and concentration (316 mol/m^3) at the bottom boundary [2]. The concentration of $\text{CO}_2(\text{g})$ is redefined as the concentration of $\text{CO}_2(\text{aq})$ in groundwater. Other parameters employed in this simulation are listed in Table 1. In Chen et al. [69], it is pointed that, for the precipitation reaction, the reactants $A(\text{aq})$ is a

kind of carbonate or bicarbonate, and $B(aq)$ is a kind of toxic cation, which is the same condition as expressed in this paper, so the value of K_c is defined from Chen et al. [69].

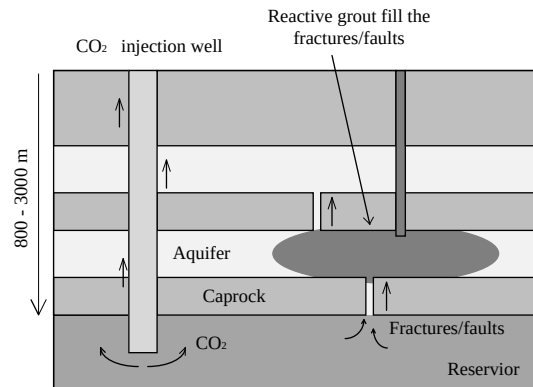


Figure 2. Diagram of reactive grouting for the CO₂ leakage remediation. Reference from [73].

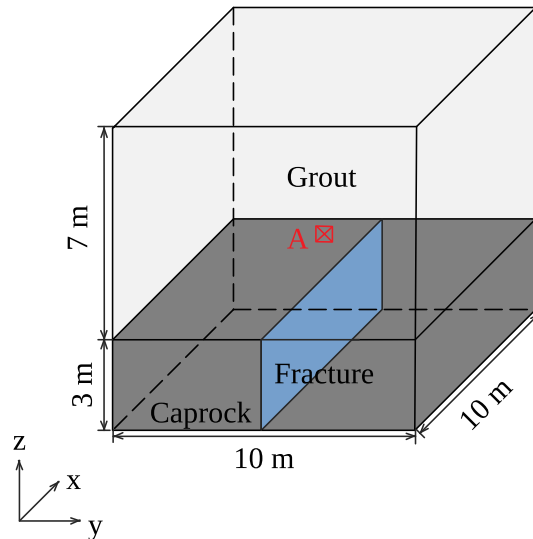


Figure 3. A 3D model for simulation the process of remedying CO₂ leakage by grouting.

Table 1. Simulation parameters for chemical precipitation reaction.

Parameters	Symbol	Unit	Value	Reference
Acid fluid viscosity	μ	Pa · s	0.0017	Ito et al. [73]
Acid fluid density	ρ	kg/m ³	1000	Ito et al. [73]
Initial porosity of aquifer	ϕ_0^{ma}		0.3	Ito et al. [73]
Intrinsic permeability of aquifer	k_0^{ma}	m ²	4×10^{-14}	Ito et al. [73]
Initial porosity of caprock	ϕ_0^{mc}		0.2375	Ito et al. [73]
Intrinsic permeability of caprock	k_0^{mc}	m ²	0	Ito et al. [73]
Molecular diffusion-dispersion coefficient	D_m	m ² /s	1.13×10^{-11}	Dávila et al. [2]
Reaction rate constant at 25 °C	k_{25}	mol/m ² · s	4.62×10^{-9}	Ito et al. [73]
Activation energy	E	J/mol	49.8×10^3	Ito et al. [73]
Gas constant	R	J/mol · J	8.314	Ito et al. [73]
Reaction equilibrium constant	K_{eq}	m ⁶ /mol ²	1.25×10^{-5}	Chen et al. [69]
Precipitation growth threshold	K_c	mol ² /m ⁶	0.8×10^5	Chen et al. [69]
Initial specific reactive surface area	A	1/m	74.8	Ito et al. [73]
Power law exponent for permeability	n		2	Ito et al. [73]
Critical porosity	ϕ_c		0.2375	Ito et al. [73]
Fracture aperture	a	m	0.01	
Fracture porosity	ϕ_0^f		1	
Fracture diffusivity	D_f	m ² /s	1.6×10^{-5}	

Since our method is quasi-implicit to calculate the total reaction rate through the concentration of reactant at the last time step, six time steps are selected to conduct the sensitivity analysis, as shown in Figure 4. The concentration of SiO_2 is chosen from the central line of the domain along the z-axis above the caprock since the model is symmetrical about the fracture plane. The total simulation time is 10 days. Figure 4 shows that the final results are convergent with the reduction of time step, and they are not sensitive to the selection of time step when the time step is less than 0.5 days.

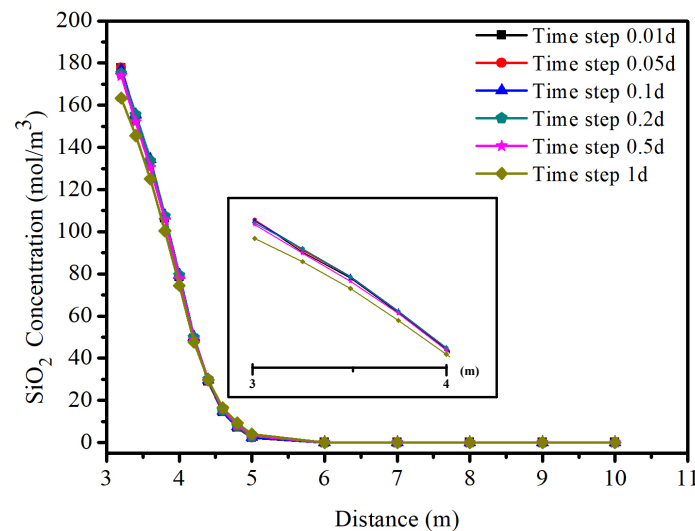


Figure 4. The influence of the time step on the UPM results.

Sensitivity analyses are further carried out with respect to the atmospheric pressure, formation temperature, the initial reactant concentration in the grout (Si), and fracture aperture. A different atmospheric pressure (P_{CO_2}) and a different formation temperature (T) will influence the solubilities of CO_2 ($\text{CO}_2(\text{g}) \rightarrow \text{CO}_2(\text{aq})$). The solubilities at each P and T are calculated from the model presented by Duan and Sun [82] and are listed in Table 2. Figure 5a–c shows the variation of precipitation concentration (SiO_2) and formation porosity with time at three different atmospheric pressures (10 bar, 50 bar, and 74 bar) and temperatures (25 °C, 70 °C, and 90 °C) in the observation Point A, as shown in Figure 3 (which is in the middle line of the domain and is 1.5 m higher than the caprock). It is observed that the quicker growth of SiO_2 concentration will cause the faster drop of porosity of formation. This is because the growth of precipitation will plug the voids of the rock. At the low atmospheric pressure, the drop of the porosity is slower than that of high pressure, since the solubilities of CO_2 at high pressure are larger. Although the reaction rate constant increases with temperature, the total variation rate decreases with the increase of temperature. At P_{CO_2} of 10 bar and T of 25 °C, the concentration of SiO_2 and porosity vary gradually with time, while they keep almost unchanged when Time is less than 200 d at T of 70 and 90 °C. At P_{CO_2} of 50 bar and 74 bar, the porosity drops quickly and tends to keep steady after 150 d.

Table 2. Concentration of $\text{CO}_2(\text{aq})$ (mol/(kg water)) at different atmospheric pressure and formation temperature. Reference from [2].

Temperature (°C)	$P_{\text{CO}_2} = 10 \text{ bar}$	$P_{\text{CO}_2} = 50 \text{ bar}$	$P_{\text{CO}_2} = 74 \text{ bar}$
25	3.16×10^{-1}	1.2×10^0	
70	1.39×10^{-1}	5.95×10^{-1}	7.88×10^{-1}
90	1.09×10^{-1}	4.95×10^{-1}	6.7×10^{-1}

Variation of porosity over time at Point A under different initial grout reactant concentration (Si) is shown in Figure 6a. When the Si concentration in the grout is 3500 mol/m^3 , the porosity is a

constant as the initial porosity. The rapid drop is observed at the Si concentration of 2000 mol/m³, while the porosity reaches the minimum value at the Si concentration of 2700 mol/m³. This is because when the concentration of reactant Si is high, once CO₂ flows into the aquifer full of grout, the reaction will happen quickly, and the volume fraction of precipitation product is large enough to clog the void to stop CO₂ further reveal into the atmosphere, as shown in Figure 6b–d. The concentration of CO₂ is zero when the height is more than 4 m. Please change the unit not to be italic if unnecessary. at the Si concentration of 3500 mol/m³ and the leakage distance of CO₂ is unchanged with time. For the low concentration of reactant solution, the pores of the formation cannot be clogged completely, and the CO₂ continues to release. But, the flow rate of CO₂ is large with the low Si concentration.

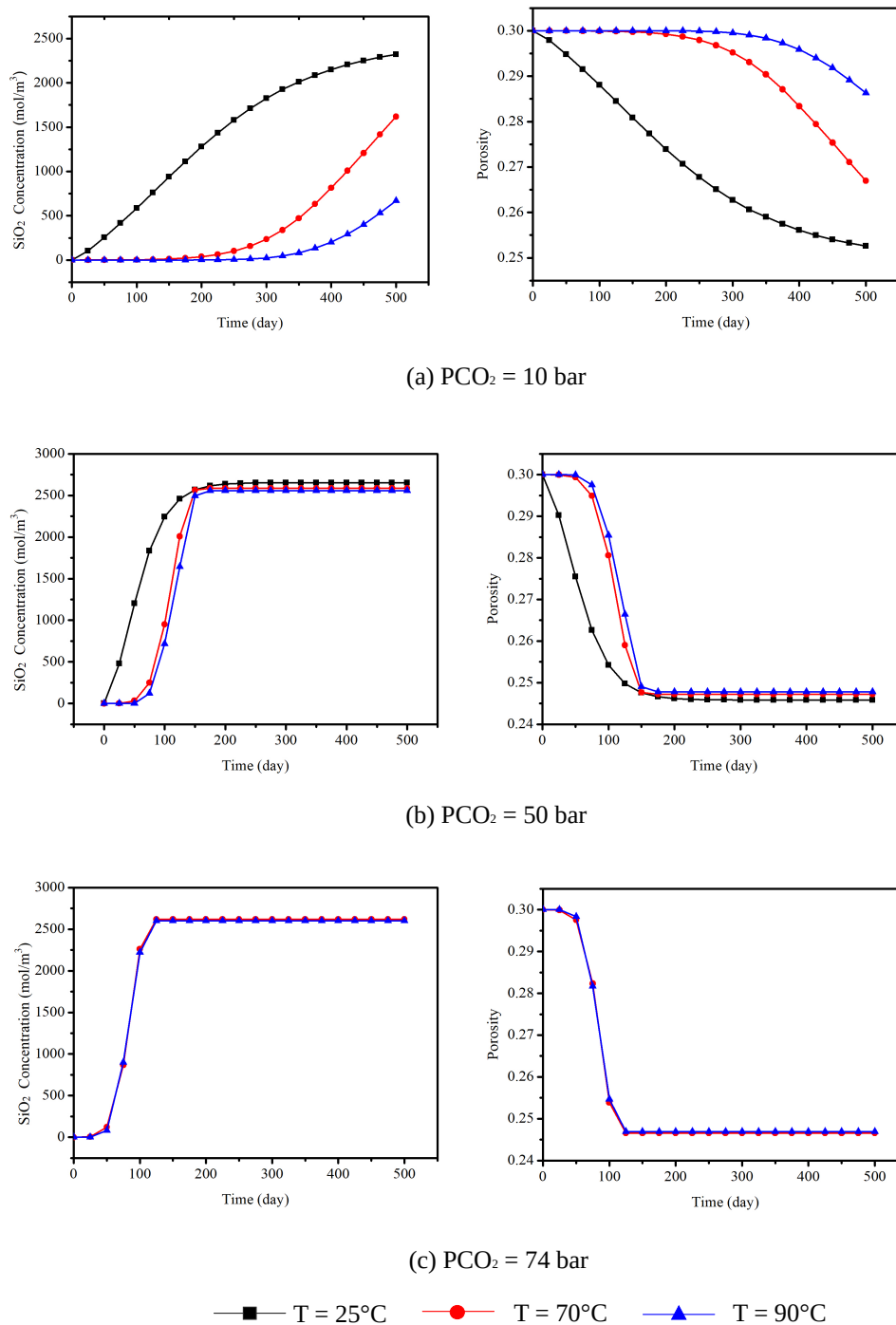


Figure 5. Variation of SiO₂ concentration and porosity with time at different atmospheric pressure and formation temperature.

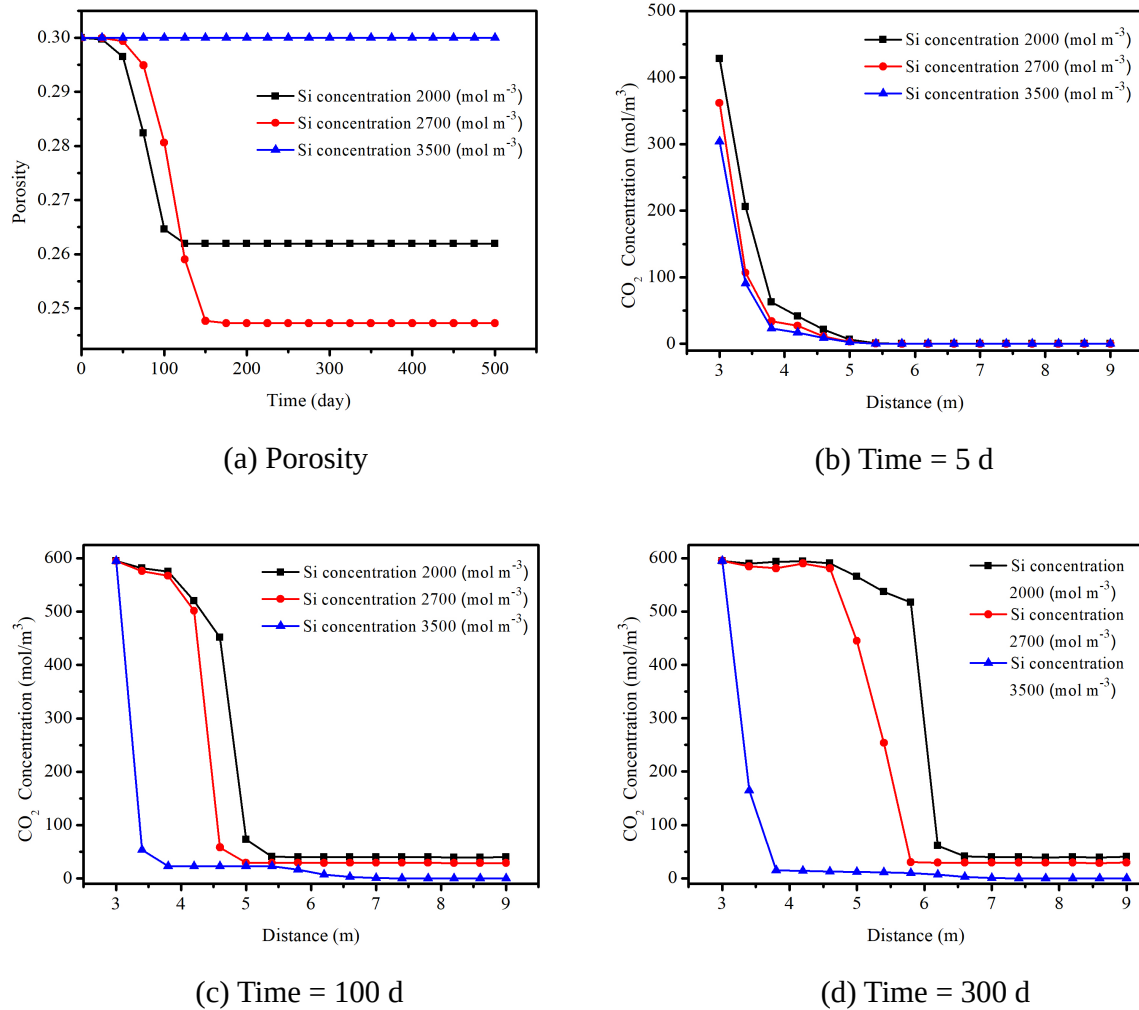


Figure 6. Influence of initial reactant concentration (Si) on CO₂ sequestration; (a) the variation of porosity with time; (b)–(d) the variation of CO₂ concentration with distance on five days, 100 days, and 300 days.

Figure 7 shows the variation of porosity at Point A considering different fracture aperture. The porosity decreases quickly with the increase of the fracture aperture. However, the rate of descent is almost same for the fracture aperture of 0.01 m and 0.1 m. This can be explained that it takes a longer time for CO₂ leakage into the aquifer when the fracture aperture is small (see Figure 7b,c). However, once the CO₂ has filled with the fracture and releases into the aquifer, the diffusion rate is almost the same (see Figure 7d). The fracture aperture can influence the CO₂ leakage effect at the initial stage. The effect of fracture dip on the CO₂ leakage and plugging effect is shown in Figure 8a,b. The dip of the fracture will influence the distribution of CO₂ in the aquifer. So, the configuration of the grout injection hole needs to be rearranged.

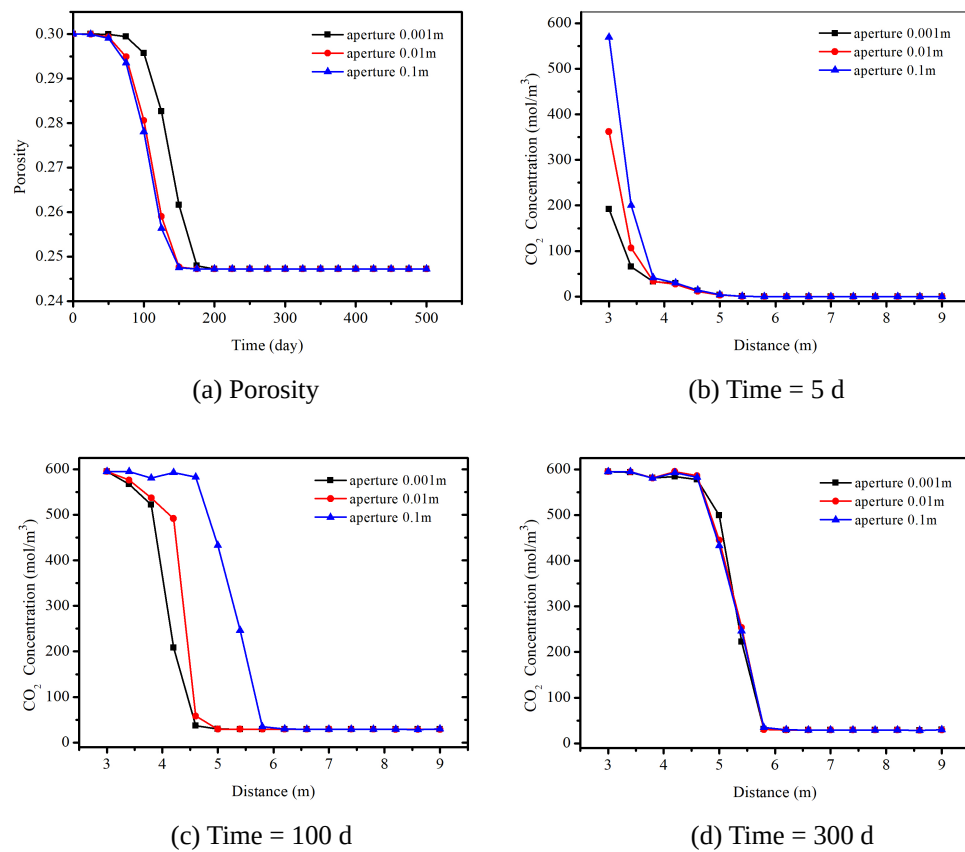


Figure 7. Influence of fracture aperture on CO₂ sequestration; (a) the variation of porosity with time; (b–d) the variation of CO₂ concentration with distance on five days, 100 days, and 300 days.

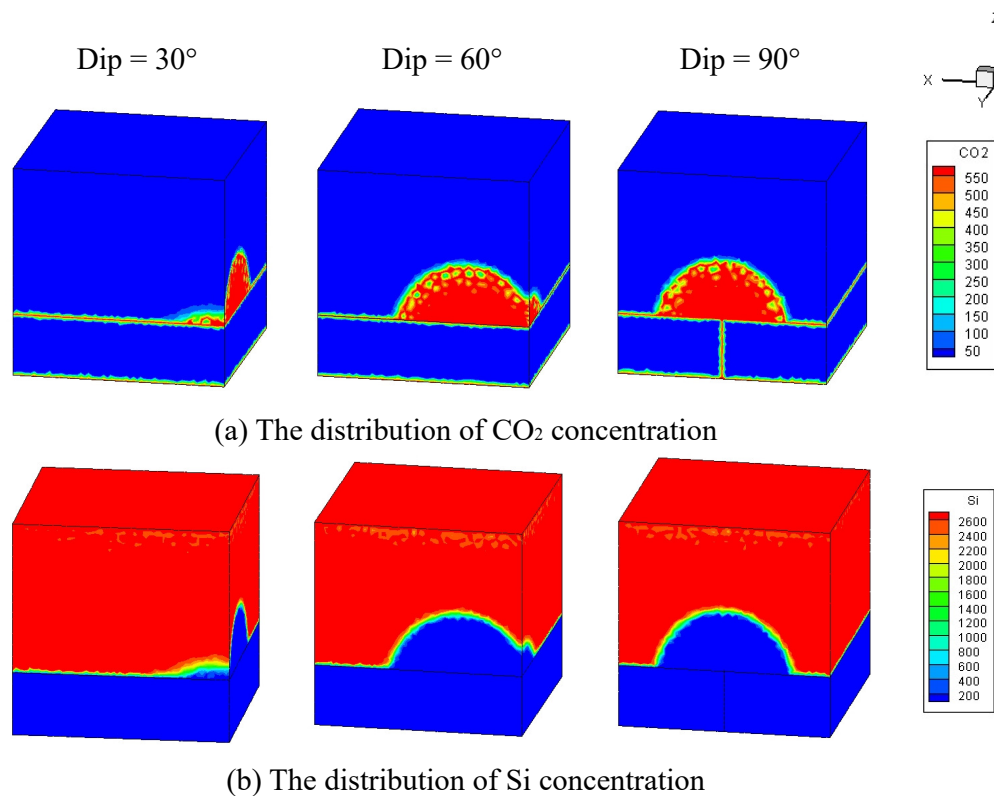


Figure 8. Numerical results of CO₂ leakage and grout reactive concentration for 365 days with different dip of fracture.

4. Simulation of CO₂ Sequestration in Rock Masses with Fracture Networks

Previous versions of fracture networks in caprock are generated in this section to simulate the CO₂ sequestration process in the reservoir. The simulation model is still a cube, and the size of model is identical to Figure 3; however, there are four large fractures connected with each other are embedded in the caprock as the main path for CO₂ leakage, as shown in Figure 9. The aquifer above the caprock is formed of sandstone with initial porosity of 0.3 and critical porosity of 0.2735 [73]. The aperture of each fracture is 0.001 m, and the intact caprock is regarded to be impermeable. The grout is silicate solution with Si concentration chosen as 3000 mol/m³ and 3500 mol/m³, respectively. CO₂ begins to release from the bottom of the model at a constant flow velocity (1.25×10^{-5} m/s). A constant pressure and a constant temperature is set along the outlet boundary. The atmospheric pressure is 50 bar, and the formation temperature is 70 °C. The total simulation time is 500 days. Other parameters are same as listed in Table 1. The fractures are discretized as triangle elements, and the rock matrix is discretized as tetrahedron elements based on an advanced adaptive mesh method [83].

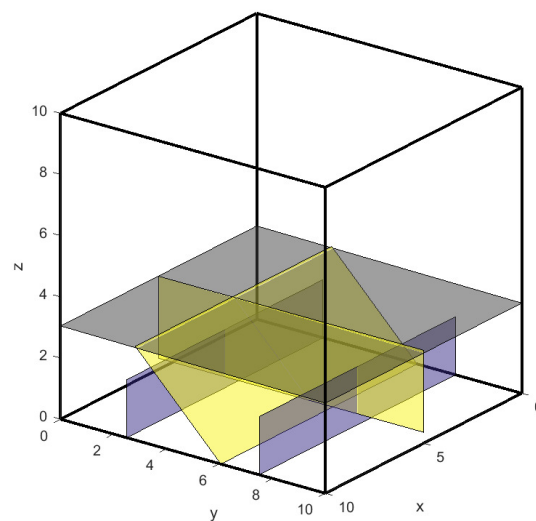


Figure 9. Three-dimensional fracture networks model in caprock for analyzing the CO₂ sequestration process (our large connected fractures)

Figure 10a–c shows the distribution of CO₂ concentration, Si concentration, and porosity at different times with the Si concentration in grout of 3000 mol/m³. When the fracture is non-penetrative in the caprock, CO₂ cannot leak into the aquifer through such a kind of crack. However, if they connected with other fractures that cut through the whole caprock, it still influences the final leakage effect. The distribution of Si concentration is adverse to that of CO₂, and the reduction of Si concentration is consistent with the drop of porosity. The region of increased CO₂ concentration and reduced Si concentration and porosity spread simultaneously in the aquifer with time. At the early stage (the simulation time is five days), the fractures are filled with CO₂ since the permeability of fractures is relatively high, which provide channels for CO₂ release with high velocity. Furthermore, the amount of CO₂ emission from two respective penetrative fractures is almost same. The distribution of CO₂ is mainly along the fracture walls, and then CO₂ releases upward. The leakage region is small and surrounds the fracture walls. With the increase of time, CO₂ continues to diffuse into the aquifer along the fractures because the voids of the aquifer are not clogged completely and the porosity does not drop to the critical value (see Figure 10c). The leakage region in x-direction is larger than that in the y-direction. This is because the amount of CO₂ leakage along the oblique fracture is influenced by the fracture that is parallel to y-axis. This can be explained by Figure 11, in which there is an obvious inflection point where CO₂ concentration starts to increase quickly at a certain time at different location. It can be seen from Figure 12 that, although CO₂ continues to leak, the concentration stops to react at a low concentration. Thus, once the Si concentration and porosity stop to reduce, it will keep the same

condition all the time. Such phenomena are caused by the reaction threshold, since the concentration of reactant is too low, and the reaction on the surface of fluid–solid cannot happen.

Figure 13 shows the variation of CO₂ concentration, Si concentration, and porosity during simulation process with the Si concentration in grout of 3500 mol/m³. It is obvious that, at the early stage, the amount of CO₂ leakage with higher Si concentration is less than that of lower Si concentration as compared with Figure 13a. As shown in Figure 13c, when CO₂ is invaded into the a region above the fracture, of which the porosity have reduced to the critical porosity, CO₂ will be successfully trapped there and stop further invasion. Thus, injecting reactive grout into the aquifer before CO₂ leakage will work well to stop CO₂ migration upward into the atmosphere through the fractures. And choosing a reasonable concentration of reactive grout according to the solubilities of CO₂(g) is necessary. Through the simulation method, the sequestration effect and CO₂ release area can be obtained to guide the arrangement of borehole of grouting.

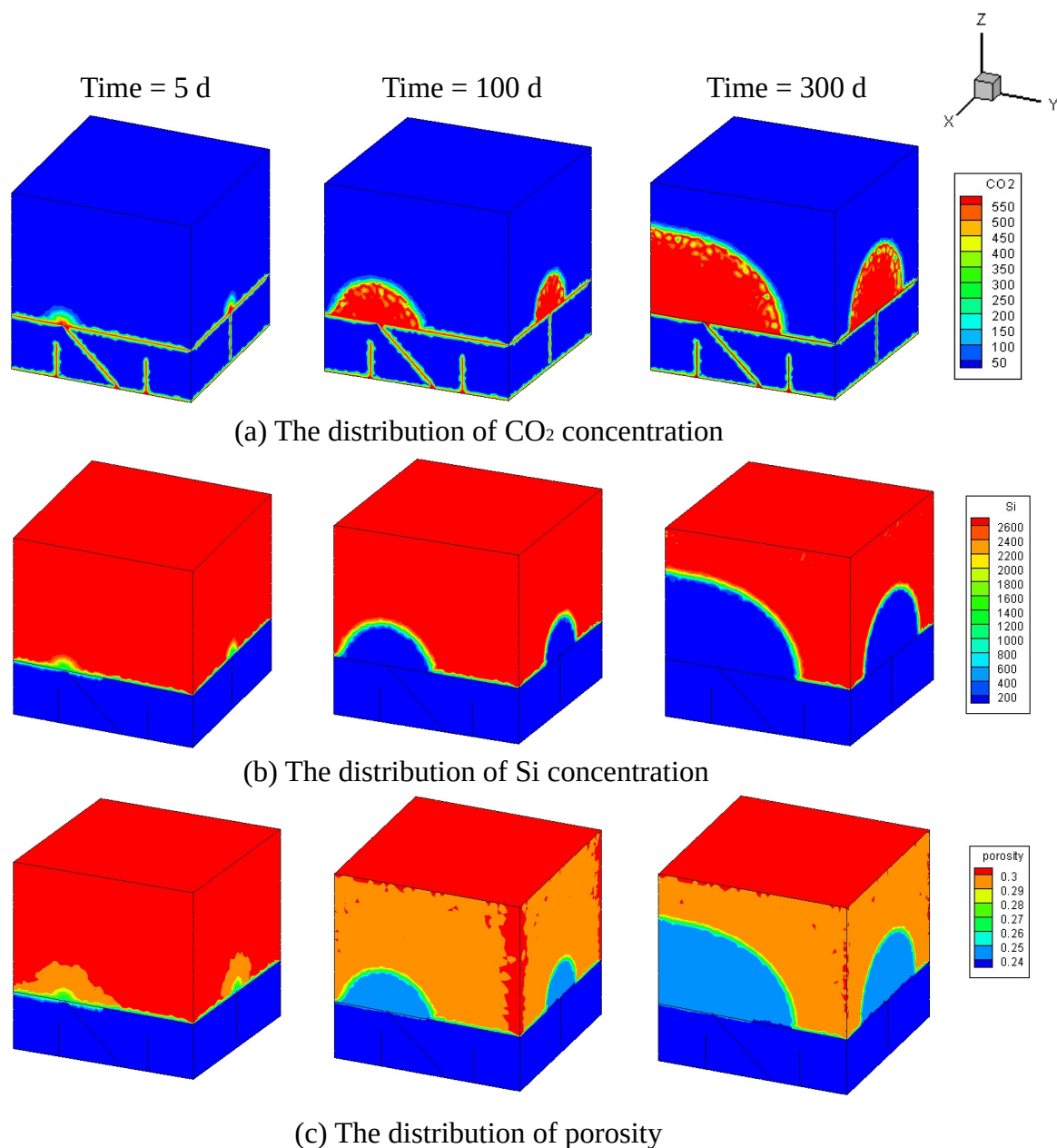


Figure 10. Numerical results of CO₂ sequestration at Si concentration of 3000 mol/m³.

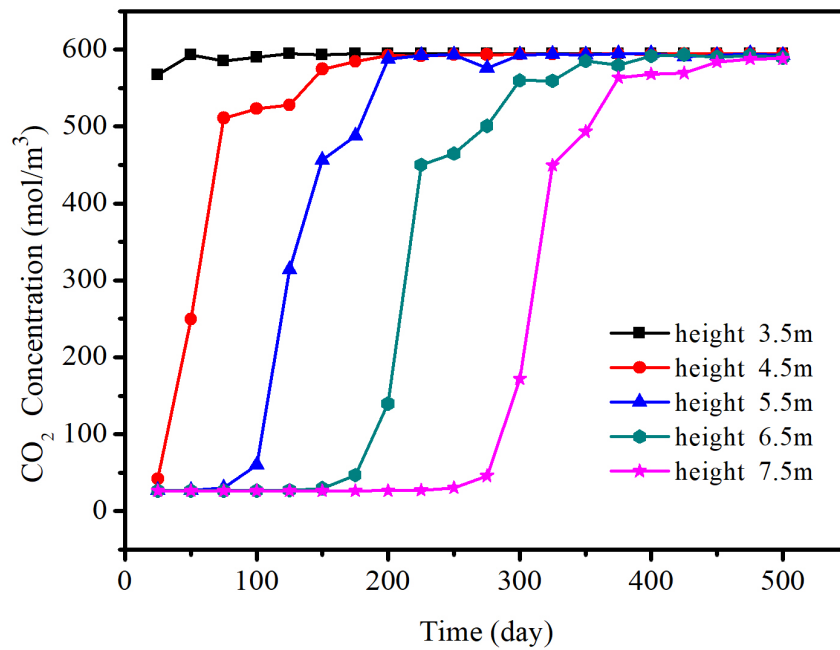


Figure 11. The variation of CO₂ concentration with time at different position at Si concentration of 3000 mol/m³.

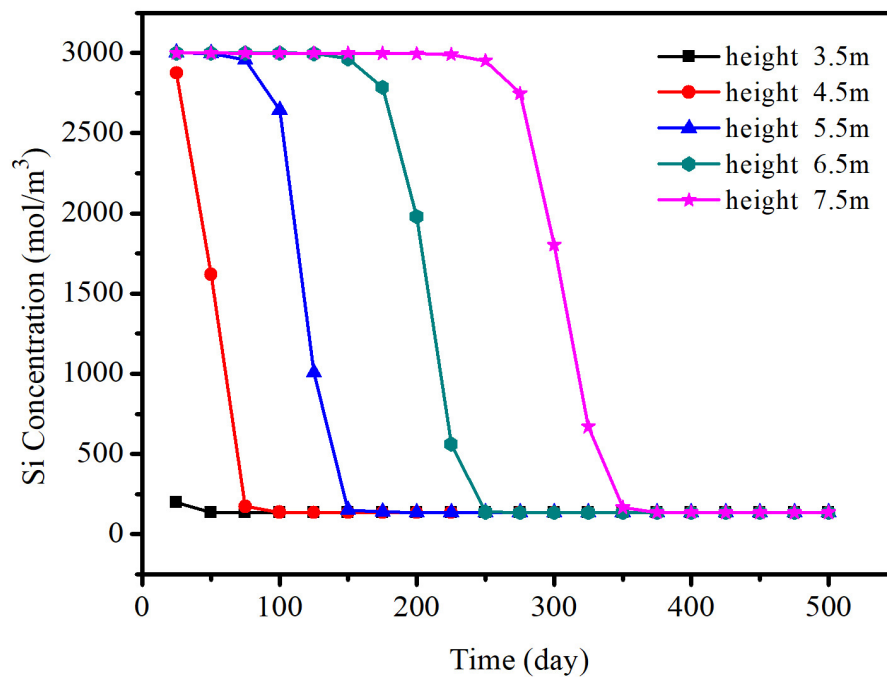


Figure 12. The variation of Si concentration with time at different position at Si concentration of 3000 mol/m³.

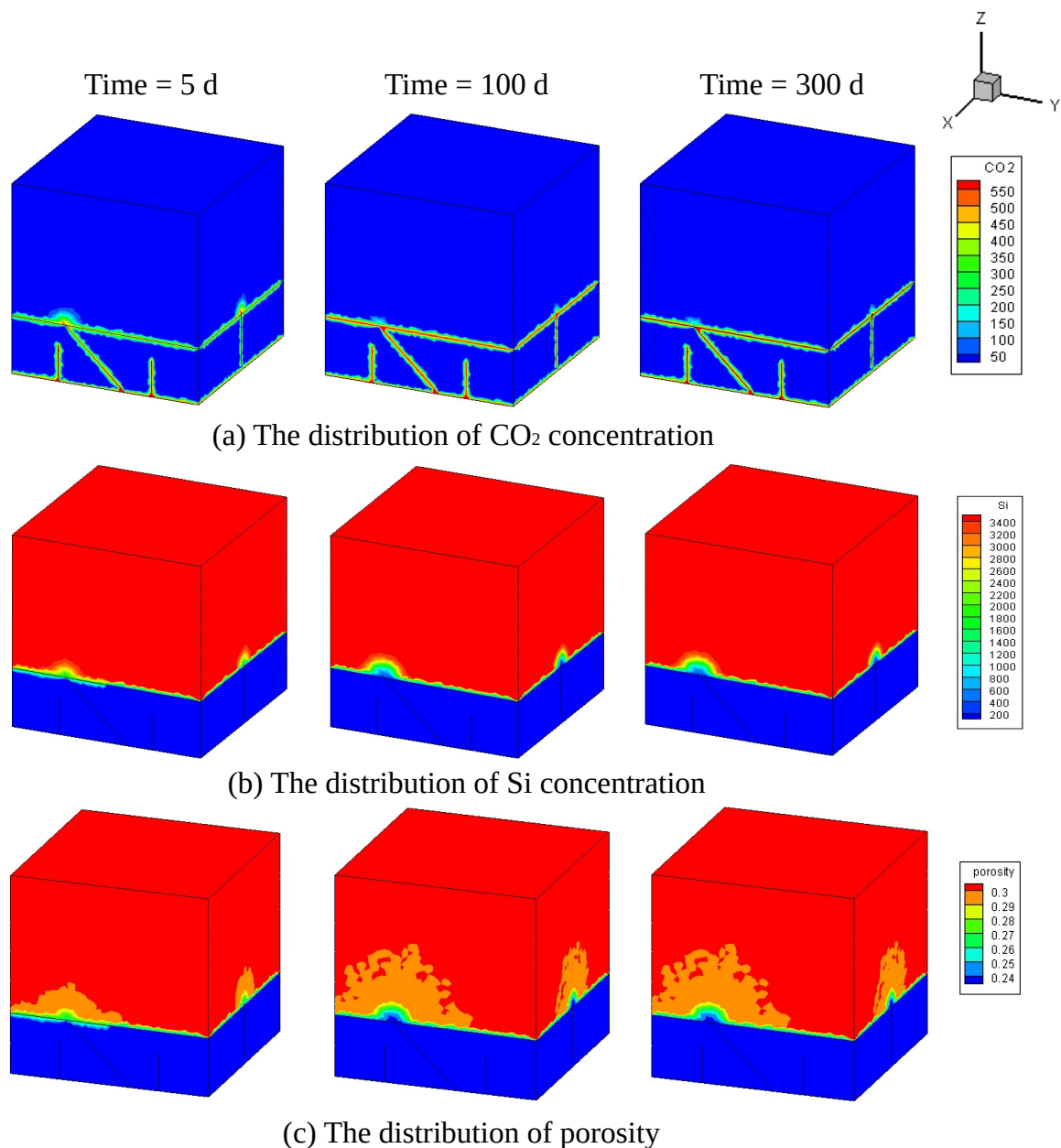


Figure 13. Numerical results of CO₂ sequestration at Si concentration of 3500 mol/m³.

5. Conclusions

The Unified Pipe-Network Method is introduced to simulate CO₂ geological sequestration in a reservoir with caprock above it that contains fractures as channels for CO₂ leakage in a 3D domain. In this model, the grout with reactive chemical solution are full of the permeable porous media located just above the caprock and can produce precipitation by a chemical reaction between the solution and dissolved CO₂. This method combines the Darcy-scale model and pore-scale model and couples the fluid flow, mass transport, and chemical reaction. The chemical module is verified by comparing with analytical results, and it is proved that the results obtained from UPM are much more accurate than other numerical results. Furthermore, due to the semi-implicit method combined in UPM, the proposed model is confirmed by performing convergence tests in respect of different time steps. The distribution of CO₂ leakage, the concentration of reactive solution Si, the concentration of precipitation, and the porosity of the formations after chemical reactive can be obtained by numerical simulation.

A sensitivity analysis that CO₂ can release from one fracture is conducted to analyze the influence of atmospheric pressure, formation temperature, the initial reactant concentration, fracture aperture, and fracture dip on CO₂ sequestration. An increase in atmospheric pressure P_{CO_2} is contributed to the chemical reaction and accelerate the reduce of porosity. At 10, 50, and 74 bar, the drop rate of porosity will decrease with the increase of temperature. Due to the mineral growth threshold, the chemical reaction cannot continue when the concentration of reactive solution is less. Increasing the reactant (Si) concentration is an effective way to improve the sequestration effect, which can effectively reduce the leakage rate of CO₂. When the Si concentration in the reactive grout is high enough, the precipitation formed in the formation can plug the pores completely and stop CO₂ being further released near the fracture. The fracture aperture can influence the distribution of CO₂ at the early stage, and the fracture dip will influence the final CO₂ release area.

A case study is carried out by establishing multi-connected fractures in the 3D caprock. At the initial stage, the connected fractures have less influence on CO₂ leakage. This 3D model can demonstrate the influence of fractures on the CO₂ emission more clearly than 2D model and help to understand the direction of CO₂ release and arrange the injection hole.

Author Contributions: Conceptualization, X.Y. and Z.S.; Methodology, Z.S., X.Y. and Y.Z.; Software, X.Y. and Z.S.; Formal Analysis, Y.Z. and Z.S.; Investigation, X.Y.; Resources, S.L.; Data Curation, W.Y.; Writing—Original Draft Preparation, X.Y. and Y.Z.; Writing—Review & Editing Y.Z.; Visualization, X.Y.; Supervision, S.L.; Project Administration, S.L.; Funding Acquisition, S.L. All authors have read and agreed to the published version of the manuscript.

Funding: This research was funded by National Key Research and Development Program of China (Grant No. 2017YFC0603001) and Key projects of the national natural science foundation of China (517340009).

Acknowledgments: This research is financially supported by National Key Research and Development Program of China (Grant No.2017YFC0603001) and Key projects of the national natural science foundation of China (517340009).

Conflicts of Interest: The authors declare no conflict of interest.

Abbreviations

The following abbreviations are used in this manuscript:

UPM Unified Pipe network Method

Appendix A. The Derivation of the Equivalent Coefficient of 3D Matrix Pipe

In the 3D UPM the rock matrix is reconstructed by tetrahedral element and the fracture is reconstructed by triangle element as shown in Figure 1 of Paper [78]. The pressures and concentrations within each tetrahedral element can be approximated by using the linear shape function as that in FEM:

$$P(x, y, z) = \sum N_k p_k \quad (k = i, j, m, n) \quad (A1)$$

$$C(x, y, z) = \sum N_k C_k \quad (k = i, j, m, n) \quad (A2)$$

where P_k and C_k are pressures and grout concentrations, respectively, and N_k is the linear shape function as in the FEM:

$$N_k = \frac{1}{6V_{ijmn}}(a_k + b_k x + c_k y + d_k z), \quad (k = i, j, m, n) \quad (A3)$$

where V_{ijmn} is the volume of the tetrahedron, and the coefficients b_k , c_k , and d_k , are dependent on the coordinates of the three nodes in each triangle element. These coefficients are represented as

$$\begin{cases} b_i = (y_n - y_j)(z_m - z_j) - (y_m - y_j)(z_n - z_j) \\ b_j = (y_m - y_i)(z_n - z_m) - (y_n - y_m)(z_m - z_i) \\ b_m = (y_j - y_n)(z_i - z_m) - (y_i - y_m)(z_j - z_n) \\ b_n = (y_i - y_m)(z_j - z_i) - (y_j - y_i)(z_i - z_m) \end{cases}$$

$$\begin{cases} c_i = (z_n - z_j)(x_m - x_j) - (z_m - z_j)(x_n - x_j) \\ c_j = (z_m - z_i)(x_n - x_m) - (z_n - z_m)(x_m - x_i) \\ c_m = (z_j - z_n)(x_i - x_m) - (z_i - z_m)(x_j - x_n) \\ c_n = (z_i - z_m)(x_j - x_i) - (z_j - z_i)(x_i - x_m) \end{cases} \quad (A4)$$

$$\begin{cases} d_i = (x_n - x_j)(y_m - y_j) - (x_m - x_j)(y_n - y_j) \\ d_j = (x_m - x_i)(y_n - y_m) - (x_n - x_m)(y_m - y_i) \\ d_m = (x_j - x_n)(y_i - y_m) - (x_i - x_m)(y_j - y_n) \\ d_n = (x_i - x_m)(y_j - y_i) - (x_j - x_i)(y_i - y_m) \end{cases}$$

The fluid flow Q_{ij}^m and mass of the solutions transported in pipe ij are equal to the flow and mass through the area $oc1fc2$ and can be calculated as

$$Q_{ij}^m = Q_{oc1fc2}^m = \int_{A_{oc1fc2}} \vec{n}_{oc1fc2} \cdot \vec{u} \, dA \quad (A5)$$

$$\dot{m}_{ij}^m = \dot{m}_{oc1fc2}^m = \int_{A_{oc1fc2}} \vec{n}_{oc1fc2} (\vec{u} \cdot \nabla C + \phi^m D_i^m \cdot \nabla C) \, dA \quad (A6)$$

where A_{oc1fc2} is the area of the face $oc1fc2$ and \vec{n}_{oc1fc2} is the unit normal vector, which can be expressed as,

$$\mathbf{n}_{of} = \frac{1}{l_{ij}} ((x_j - x_i) \vec{x} + (y_j - y_i) \vec{y} + (z_j - z_i) \vec{z}) \quad (A7)$$

Therefore, the equivalent conductance coefficient and equivalent diffusion coefficient for 3D matrix pipe is derived as:

$$K_{ij}^m = \frac{A_{oc1fc2} K_i^m}{l_{ij} \mu} \quad (A8)$$

$$D_{ij}^m = \frac{\phi_i^m A_{oc1fc2} D_i^m}{l_{ij}} \quad (A9)$$

Appendix B. The Derivation of the Equivalent Coefficient of 3D Fracture Pipe

The linear shape function of 3D pipe network N_k with b_k, c_k is expressed as

$$N_k = \frac{1}{2A_{ijm}} (a_k + b_k x + c_k y), (k = i, j, m) \quad (A10)$$

$$\begin{cases} b_i = y_j - y_m \\ b_j = y_m - y_i \\ b_m = y_i - y_j \end{cases} \quad (A11)$$

$$\begin{cases} c_i = x_m - x_j \\ c_j = x_i - x_m \\ c_m = x_j - x_i \end{cases}$$

Therefore, the equivalent conductance coefficient and equivalent diffusion coefficient for 3D fracture pipe is derived as:

$$K_{ij}^f = \frac{A_{of} K_i^f}{l_{ij} \mu} = \frac{l_{of} a^3}{l_{ij} \mu} \quad (A12)$$

$$D_{ij}^f = \frac{\phi_i^f A_{of} D_i^f}{l_{ij}} = \frac{\phi_i^f l_{of} D_i^f a}{l_{ij}} \quad (A13)$$

References

- Wasch, L.J.; Wollenweber, J.; Neele, F.; Fleury, M. Mitigating CO₂ leakage by immobilizing CO₂ into solid reaction products. *Energy Procedia* **2017**, *114*, 4214–4226. [\[CrossRef\]](#)
- Dávila, G.; Cama, J.; Gali, S.; Luquot, L.; Soler, J.M. Efficiency of magnesium hydroxide as engineering seal in the geological sequestration of CO₂. *Int. J. Greenh. Gas Control* **2016**, *48*, 171–185. [\[CrossRef\]](#)
- Dalkhaa, C.; Shevalier, M.; Nightingale, M.; Mayer, B. 2-d reactive transport modeling of the fate of CO₂ injected into a saline aquifer in the wabamun lake area, alberta, canada. *Appl. Geochem.* **2013**, *38*, 10–23. [\[CrossRef\]](#)
- Sahimi, M. *Flow and Transport in Porous Media and Fractured Rock: From Classical Methods to Modern Approaches*; John Wiley & Sons: Hoboken, NJ, USA, 2011.
- Seifert, D.; Engesgaard, P. Sand box experiments with bioclogging of porous media: Hydraulic conductivity reductions. *J. Contam. Hydrol.* **2012**, *136*, 1–9. [\[CrossRef\]](#)
- Kutchko, B.G.; Strazisar, B.R.; Dzombak, D.A.; Lowry, G.V.; Thaulow, N. Degradation of well cement by CO₂ under geologic sequestration conditions. *Environ. Sci. Technol.* **2007**, *41*, 4787–4792. [\[CrossRef\]](#)
- Dewaele, P.; Reardon, E.; Dayal, R. Permeability and porosity changes associated with cement grout carbonation. *Cement Concr. Res.* **1991**, *21*, 441–454. [\[CrossRef\]](#)
- Scherer, G.W.; Celia, M.A.; Prevost, J.-H.; Bachu, S.; Bruant, R.; Duguid, A.; Fuller, R.; Gasda, S.E.; Radonjic, M.; Vichit-Vadakan, W. Leakage of CO₂ through abandoned wells: Role of corrosion of cement. In *Carbon Dioxide Capture for Storage in Deep Geologic Formations*; Elsevier: Amsterdam, The Netherlands, 2015; pp. 827–848.
- Bachu, S.; Bennion, D.B. Experimental assessment of brine and/or CO₂ leakage through well cements at reservoir conditions. *Int. J. Greenh. Gas Control* **2009**, *3*, 494–501. [\[CrossRef\]](#)
- Duguid, A. An estimate of the time to degrade the cement sheath in a well exposed to carbonated brine. *Energy Procedia* **2009**, *1*, 3181–3188. [\[CrossRef\]](#)
- Luquot, L.; Abdoulghafour, H.; Gouze, P. Hydro-dynamically controlled alteration of fractured portland cements flowed by CO₂-rich brine. *Int. J. Greenh. Gas Control* **2013**, *16*, 167–179. [\[CrossRef\]](#)
- Babaei, M.; Sedighi, M. Impact of phase saturation on wormhole formation in rock matrix acidizing. *Chem. Eng. Sci.* **2018**, *177*, 39–52. [\[CrossRef\]](#)
- Ellery, A.J.; Simpson, M.J. An analytical method to solve a general class of nonlinear reactive transport models. *Chem. Eng. J.* **2011**, *169*, 313–318. [\[CrossRef\]](#)
- Kim, Y.; Wan, J.; Kneafsey, T.J.; Tokunaga, T.K. Dewetting of silica surfaces upon reactions with supercritical CO₂ and brine: Pore-scale studies in micromodels. *Environ. Sci. Technol.* **2012**, *46*, 4228–4235. [\[CrossRef\]](#)
- Noiriel, C.; Gouze, P.; Bernard, D. Investigation of porosity and permeability effects from microstructure changes during limestone dissolution. *Geophys. Res. Lett.* **2004**, *31*. [\[CrossRef\]](#)
- Noiriel, C.; Bernard, D.; Gouze, P.; Thibault, X. Hydraulic properties and microgeometry evolution accompanying limestone dissolution by acidic water. *Oil Gas Sci. Technol.* **2005**, *60*, 177–192. [\[CrossRef\]](#)
- Li, L.; Peters, C.A.; Celia, M.A. Upscaling geochemical reaction rates using pore-scale network modeling. *Adv. Water Resour.* **2006**, *29*, 1351–1370. [\[CrossRef\]](#)
- De Anna, P.; Dentz, M.; Tartakovsky, A.; Le Borgne, T. The filamentary structure of mixing fronts and its control on reaction kinetics in porous media flows. *Geophys. Res. Lett.* **2014**, *41*, 4586–4593. [\[CrossRef\]](#)
- Algive, L.; Bekri, S.; Robin, M.; Vizika, O. Reactive transport: Experiments and pore network modelling. In *Proceedings of the International Symposium of the Society of Core Analysts*, Calgary, AB, Canada, 10–12 September 2007; pp. 10–12.

20. Gramling, C.M.; Harvey, C.F.; Meigs, L.C. Reactive transport in porous media: A comparison of model prediction with laboratory visualization. *Environ. Sci. Technol.* **2002**, *36*, 2508–2514. [\[CrossRef\]](#)
21. Raje, D.S.; Kapoor, V. Experimental study of bimolecular reaction kinetics in porous media. *Environ. Sci. Technol.* **2000**, *34*, 1234–1239. [\[CrossRef\]](#)
22. Lagneau, V. Influence des Processus géochimiques sur le Transport en Milieu Poreux—Application au Colmatage de Barrières de Confinement Potentielles Dans un Stockage en Formation Géologique. Ph.D. Thesis, École des Mines de Paris, Paris, France, 2000.
23. Emmanuel, S.; Berkowitz, B. Mixing-induced precipitation and porosity evolution in porous media. *Adv. Water Resour.* **2005**, *28*, 337–344. [\[CrossRef\]](#)
24. ATartakovsky, M.; Redden, G.; Lichtner, P.C.; Scheibe, T.D.; Meakin, P. Mixing-induced precipitation: Experimental study and multiscale numerical analysis. *Water Resour. Res.* **2008**, *44*. [\[CrossRef\]](#)
25. Chasset, C.; Jarsjö, J.; Erlström, M.; Cvetkovic, V.; Destouni, G. Scenario simulations of CO₂ injection feasibility, plume migration and storage in a saline aquifer, Scania, Sweden. *Int. J. Greenh. Gas Control* **2011**, *5*, 1303–1318. [\[CrossRef\]](#)
26. De Windt, L.; Pellegrini, D.; van Der Lee, J. Coupled modeling of cement/claystone interactions and radionuclide migration. *J. Contam. Hydrol.* **2004**, *68*, 165–182. [\[CrossRef\]](#)
27. Gaucher, E.C.; Blanc, P. Cement/clay interactions—A review: Experiments, natural analogues, and modeling. *Waste Manag.* **2006**, *26*, 776–788. [\[CrossRef\]](#)
28. Kosakowski, G.; Berner, U. The evolution of clay rock/cement interfaces in a cementitious repository for low-and intermediate level radioactive waste. *Phys. Chem. Earth Parts A/B/C* **2013**, *64*, 65–86. [\[CrossRef\]](#)
29. Xu, T.; Apps, J.A.; Pruess, K.; Yamamoto, H. Numerical modeling of injection and mineral trapping of CO₂ with H₂S and SO₂ in a sandstone formation. *Chem. Geol.* **2007**, *242*, 319–346. [\[CrossRef\]](#)
30. Gaus, I. Role and impact of CO₂–rock interactions during CO₂ storage in sedimentary rocks. *Int. J. Greenh. Gas Control* **2010**, *4*, 73–89. [\[CrossRef\]](#)
31. Gaus, I.; Audigane, P.; André, L.; Lions, J.; Jacquemet, N.; Durst, P.; Czernichowski-Lauriol, I.; Azaroual, M. Geochemical and solute transport modelling for CO₂ storage, what to expect from it? *Int. J. Greenh. Gas Control* **2008**, *2*, 605–625. [\[CrossRef\]](#)
32. Steefel, C.I.; Lasaga, A.C. A coupled model for transport of multiple chemical species and kinetic precipitation/dissolution reactions with application to reactive flow in single phase hydrothermal systems. *Am. J. Sci.* **1994**, *294*, 529–592. [\[CrossRef\]](#)
33. Pollock, D.W. Semianalytical computation of path lines for finite-difference models. *Groundwater* **1988**, *26*, 743–750. [\[CrossRef\]](#)
34. Voss, C.I. *A finite-Element Simulation Model for Saturated-Unsaturated, Fluid-Density-Dependent Ground-Water Flow with Energy Transport or Chemically-Reactive Single-Species Solute Transport*; US Geological Survey: Reston, VA, USA, 1984; Volume 84.
35. Löhner, R.; Morgan, K.; Peraire, J.; Vahdati, M. Finite element flux-corrected transport (fem-fct) for the euler and navier–stokes equations. *Int. J. Numer. Methods Fluids* **1987**, *7*, 1093–1109. [\[CrossRef\]](#)
36. Trefry, M.G.; Muffels, C. Feflow: A finite-element ground water flow and transport modeling tool. *Groundwater* **2007**, *45*, 525–528. [\[CrossRef\]](#)
37. Diersch, H.-J.G. *FEFLOW: Finite Element Modeling of Flow, Mass and Heat Transport in Porous and Fractured Media*; Springer Science & Business Media: Berlin/Heidelberg, Germany, 2013.
38. Geiger, S.; Roberts, S.; Matthäi, S.; Zoppou, C.; Burri, A. Combining finite element and finite volume methods for efficient multiphase flow simulations in highly heterogeneous and structurally complex geologic media. *Geofluids* **2004**, *4*, 284–299. [\[CrossRef\]](#)
39. Saripalli, K.P.; Meyer, P.D.; Bacon, D.H.; Freedman, V.L. Changes in hydrologic properties of aquifer media due to chemical reactions: A review. *Crit. Rev. Environ. Sci. Technol.* **2001**, *31*, 311–349. [\[CrossRef\]](#)
40. Luo, H.; Quintard, M.; Debenest, G.; Laouafa, F. Properties of a diffuse interface model based on a porous medium theory for solid–liquid dissolution problems. *Comput. Geosci.* **2012**, *16*, 913–932. [\[CrossRef\]](#)
41. Kang, Q.; Chen, L.; Valocchi, A.J.; Viswanathan, H.S. Pore-scale study of dissolution-induced changes in permeability and porosity of porous media. *J. Hydrol.* **2014**, *517*, 1049–1055. [\[CrossRef\]](#)
42. Kang, Q.; Lichtner, P.C.; Zhang, D. Lattice boltzmann pore-scale model for multicomponent reactive transport in porous media. *J. Geophys. Res. Solid Earth* **2006**, *111*. [\[CrossRef\]](#)

43. Parmigiani, A.; Huber, C.; Bachmann, O.; Chopard, B. Pore-scale mass and reactant transport in multiphase porous media flows. *J. Fluid Mech.* **2011**, *686*, 40–76. [\[CrossRef\]](#)
44. Maloszewski, P.; Zuber, A. Tracer experiments in fractured rocks: Matrix diffusion and the validity of models. *Water Resour. Res.* **1993**, *29*, 2723–2735. [\[CrossRef\]](#)
45. Sudicky, E.; Frind, E. Contaminant transport in fractured porous media: Analytical solutions for a system of parallel fractures. *Water Resour. Res.* **1982**, *18*, 1634–1642. [\[CrossRef\]](#)
46. Bigi, S.; Battaglia, M.; Alemanni, A.; Lombardi, S.; Campana, A.; Borisova, E.; Loizzo, M. CO₂ flow through a fractured rock volume: Insights from field data, 3d fractures representation and fluid flow modeling. *Int. J. Greenh. Gas Control* **2013**, *18*, 183–199. [\[CrossRef\]](#)
47. Lee, I.-H.; Ni, C.-F. Fracture-based modeling of complex flow and CO₂ migration in three-dimensional fractured rocks. *Comput. Geosci.* **2015**, *81*, 64–77. [\[CrossRef\]](#)
48. Pan, P.-Z.; Rutqvist, J.; Feng, X.-T.; Yan, F. Modeling of caprock discontinuous fracturing during CO₂ injection into a deep brine aquifer. *Int. J. Greenh. Gas Control* **2013**, *19*, 559–575. [\[CrossRef\]](#)
49. Ren, F.; Ma, G.; Wang, Y.; Fan, L. Pipe network model for unconfined seepage analysis in fractured rock masses. *Int. J. Rock Mech. Min. Sci.* **2016**, *88*, 183–196. [\[CrossRef\]](#)
50. Ren, F.; Ma, G.; Wang, Y.; Fan, L.; Zhu, H. Two-phase flow pipe network method for simulation of CO₂ sequestration in fractured saline aquifers. *Int. J. Rock Mech. Min. Sci.* **2017**, *98*, 39–53. [\[CrossRef\]](#)
51. Ma, G.; Chen, Y.; Jin, Y.; Wang, H. Modelling temperature-influenced acidizing process in fractured carbonate rocks. *Int. J. Rock Mech. Min. Sci.* **2018**, *105*, 73–84. [\[CrossRef\]](#)
52. Ma, G.; Li, T.; Wang, Y.; Chen, Y. A semi-continuum model for numerical simulations of mass transport in 3-d fractured rock masses. *Rock Mech. Rock Eng.* **2019**, 1–20. [\[CrossRef\]](#)
53. Zhang, Y.; Pichler, C.; Yuan, Y.; Zeiml, M.; Lackner, R. Micromechanics-based multifield framework for early-age concrete. *Eng. Struct.* **2013**, *47*, 16–24. [\[CrossRef\]](#)
54. Pesavento, F.; Gawin, D.; Wyrzykowski, M.; Schrefler, B.; Simoni, L. Modeling alkali-silica reaction in non-isothermal, partially saturated cement based materials. *Comput. Methods Appl. Mech. Eng.* **2012**, *225*–*228*, 95–115. [\[CrossRef\]](#)
55. Zhang, Y.; Zeiml, M.; Pichler, C.; Lackner, R. Model-based risk assessment of concrete spalling in tunnel linings under fire loading. *Eng. Struct.* **2014**, *77*, 207–215. [\[CrossRef\]](#)
56. Gawin, D.; Pesavento, F.; Schrefler, B. Hygro-thermo-chemo-mechanical modelling of concrete at early ages and beyond. Part I: Hydration and hygro-thermal phenomena. *Int. J. Numer. Methods Eng.* **2006**, *67*, 299–331. [\[CrossRef\]](#)
57. Zhang, Y.; Zeiml, M.; Maier, M.; Yuan, Y.; Lackner, R. Fast assessing spalling risk of tunnel linings under rabbit fire: From a coupled thermo-hydro-chemo-mechanical model towards an estimation method. *Eng. Struct.* **2017**, *142*, 1–19. [\[CrossRef\]](#)
58. Zhang, Y.; Lackner, R.; Zeiml, M.; Mang, H. Strong discontinuity embedded approach with standard SOS formulation: Element formulation, energy-based crack-tracking strategy, and validations. *Comput. Methods Appl. Mech. Eng.* **2015**, *287*, 335–366. [\[CrossRef\]](#)
59. Wu, J.-Y. A unified phase-field theory for the mechanics of damage and quasi-brittle failure. *J. Mech. Phys. Solids* **2017**, *103*, 72–99. [\[CrossRef\]](#)
60. Zhang, Y.; Zhuang, X. Cracking elements: A self-propagating strong discontinuity embedded approach for quasi-brittle fracture. *Finite Elem. Anal. Des.* **2018**, *144*, 84–100. [\[CrossRef\]](#)
61. Wu, J.-Y. A geometrically regularized gradient-damage model with energetic equivalence. *Comput. Methods Appl. Mech. Eng.* **2018**, *328*, 612–637. [\[CrossRef\]](#)
62. Ren, H.; Zhuang, X.; Cai, Y.; Rabczuk, T. Dual-horizon peridynamics. *Int. J. Numer. Methods Eng.* **2016**, *108*, 1451–1476. [\[CrossRef\]](#)
63. Zhang, Y.; Zhuang, X. Cracking elements method for dynamic brittle fracture. *Theor. Appl. Fract. Mech.* **2019**, *102*, 1–9. [\[CrossRef\]](#)
64. Rabczuk, T.; Ren, H. A peridynamics formulation for quasi-static fracture and contact in rock. *Eng. Geol.* **2017**, *225*, 42–48. [\[CrossRef\]](#)
65. Zhang, Y.; Gao, Z.; Li, Y.; Zhuang, X. On the crack opening and energy dissipation in a continuum based disconnected crack model. *Finite Elem. Anal. Des.* **2019**. [\[CrossRef\]](#)

66. Nikolić, M.; Do, X.N.; Ibrahimbegovic, A.; Nikolić, Ž. Crack propagation in dynamics by embedded strong discontinuity approach: Enhanced solid versus discrete lattice model. *Comput. Methods Appl. Mech. Eng.* **2018**, *340*, 480–499. [CrossRef]
67. Haerberlein, F. Time Space Domain Decomposition Methods for Reactive Transport-Application to CO₂ Geological Storage. 2011. Available online: <https://tel.archives-ouvertes.fr/tel-00634507/file/transparents.pdf> (accessed on 20 October 2019).
68. Zimmerman, R.W.; Bodvarsson, G.S. Hydraulic conductivity of rock fractures. *Transp. Porous Media* **1996**, *23*, 1–30. [CrossRef]
69. Chen, L.; Kang, Q.; Carey, B.; Tao, W.-Q. Pore-scale study of diffusion–reaction processes involving dissolution and precipitation using the lattice boltzmann method. *Int. J. Heat Mass Transf.* **2014**, *75*, 483–496. [CrossRef]
70. Lasaga, A.C. Chemical kinetics of water-rock interactions. *J. Geophys. Res. Solid Earth* **1984**, *89*, 4009–4025. [CrossRef]
71. Xu, T.; Apps, J.A.; Pruess, K. Mineral sequestration of carbon dioxide in a sandstone–shale system. *Chem. Geol.* **2005**, *217*, 295–318. [CrossRef]
72. Liu, M.; Mostaghimi, P. Numerical simulation of fluid-fluid-solid reactions in porous media. *Int. J. Heat Mass Transf.* **2018**, *120*, 194–201. [CrossRef]
73. Ito, T.; Xu, T.; Tanaka, H.; Taniuchi, Y.; Okamoto, A. Possibility to remedy CO₂ leakage from geological reservoir using CO₂ reactive grout. *Int. J. Greenh. Gas Control* **2014**, *20*, 310–323. [CrossRef]
74. Verma, A.; Pruess, K. Thermohydrological conditions and silica redistribution near high-level nuclear wastes emplaced in saturated geological formations. *J. Geophys. Res. Solid Earth* **1988**, *93*, 1159–1173. [CrossRef]
75. Lichtner, P.C. The quasi-stationary state approximation to coupled mass transport and fluid-rock interaction in a porous medium. *Geochim. Cosmochim. Acta* **1988**, *52*, 143–165. [CrossRef]
76. Ren, F.; Ma, G.; Fu, G.; Zhang, K. Investigation of the permeability anisotropy of 2d fractured rock masses. *Eng. Geol.* **2015**, *196*, 171–182. [CrossRef]
77. Ren, F.; Ma, G.; Wang, Y.; Li, T.; Zhu, H. Unified pipe network method for simulation of water flow in fractured porous rock. *J. Hydrol.* **2017**, *547*, 80–96. [CrossRef]
78. Sun, Z.; Yan, X.; Han, W.; Ma, G.; Zhang, Y. Simulating the filtration effects of cement-grout in fractured porous media with the 3d unified pipe-network method. *Processes* **2019**, *7*, 46. [CrossRef]
79. Sun, Z.; Yan, X.; Liu, R.; Xu, Z.; Li, S.; Zhang, Y. Transient analysis of grout penetration with time-dependent viscosity inside 3d fractured rock mass by unified pipe-network method. *Water* **2018**, *10*, 1122. [CrossRef]
80. Poskozim, P.S. General chemistry, principles and modern applications, (petrucci, ralph h.; harwood, william s.) and general chemistry, (whitten, kenneth w.; davis, raymond e.; peck, m. larry). *J. Chem. Educ.* **1997**. [CrossRef]
81. Alhashmi, Z.; Blunt, M.; Bijeljic, B. Predictions of dynamic changes in reaction rates as a consequence of incomplete mixing using pore scale reactive transport modeling on images of porous media. *J. Contam. Hydrol.* **2015**, *179*, 171–181. [CrossRef] [PubMed]
82. Duan, Z.; Sun, R. An improved model calculating CO₂ solubility in pure water and aqueous nacl solutions from 273 to 533 k and from 0 to 2000 bar. *Chem. Geol.* **2003**, *193*, 257–271. [CrossRef]
83. Wang, Y.; Ma, G.; Ren, F.; Li, T. A constrained delaunay discretization method for adaptively meshing highly discontinuous geological media. *Comput. Geosci.* **2017**, *109*, 134–148. [CrossRef]

